Compact intracavity mid-infrared upconversion detector: a systematic study

Kashak, Tyler; Flannigan, Liam; Atwi, Ali; Poitras, Daniel; Xu, Chang-qing

Publisher's version / Version de l'éditeur:
https://doi.org/10.1364/OPTCON.533926
Optics Continuum, 3, 9, pp. 1660-1678, 2024-09-11

Research Article Vol. 3, No. 9 / 15 Sep 2024 / Optics Continuum 1660
OPTICS CONTINUUM

Compact intracavity mid-infrared upconversion detector – a systematic study

TYLER KASHAK,[1,†] LIAM FLANNIGAN,[1,†,*] ALI ATWI,[1] DANIEL POITRAS,[2] AND CHANG-QING XU[1]

[1]McMaster Engineering Physics, Department of Engineering, 1280 Main Street West, Hamilton, ON, L8S4L8, Canada
[2]Advanced Electronics and Photonics Research Center, National Research Council Canada, Ottawa, ON K1A 0R6, Canada
[†]These authors contributed equally to this work
[*]flannilg@mcmaster.ca

Abstract: Mid-IR light detection based on intracavity upconversion using a compact structure has been studied experimentally and theoretically. The mid-IR detector consists of a 47.5 mm MgO doped periodically poled lithium niobate crystal placed in a resonant cavity of a 1064 nm diode-pumped Nd:YVO_4 laser to enhance efficiency. The generated 1064 nm light is mixed with a mid-infrared source emitting at 3469 nm using an intracavity dichroic mirror. This produces short wave infrared 814.2 nm light via sum frequency generation (SFG). The upconverted light overlaps with the high responsivity for commercial off-the-shelf silicon photodetectors, enabling high speed and high sensitivity detection, surpassing direct mid-infrared detection. The lowest power detected was 150 nW, and the theoretical noise equivalent power for state-of-the-art Si detectors is $1.7 \cdot f\mathrm{W}/\sqrt{\mathrm{Hz}}$. The free-running cavity requires no active stabilization, and the total packaged prototype size is $3.75 \times 3.0 \times 8.0$ cm, which is relatively compact. An experimental power conversion efficiency of up to 36.0% is observed, which agrees well with theoretical simulations. A systematic theoretical study is performed to investigate the potential for further device optimization.

1. Introduction

Optical free space communication has benefitted from rapid development and an increase in interest from the broader scientific community in recent years. It is clear to see why, given the benefits of optical carriers over radio: larger bandwidths, higher link security, smaller size, weight and power (SWaP) for transmitters and receivers, and lighter regulatory burden [1]. Most current efforts focus on using the short-wave infrared (SWIR), specifically the C-band (1525-1565 nm), for long distance links. This is in large part due to the availability of mature off-the-shelf sources and detectors with high speed and sensitivity due to advances in fiber telecommunications. While the SWIR will no doubt serve as the backbone of free space optical communication, it is not without problems. Atmospheric effects such as scattering and turbulence/scintillation, as well as weather including fog and haze can greatly reduce link availability. One potential mitigation technique is to move to longer wavelengths that still fall within one of the atmospheric transmission windows. A promising candidate is the mid infrared (mid-IR, 3-5 microns) which greatly reduces scattering and scintillation, and can relax requirements for adaptive optics over long distances [2,3].

One of the major challenges posed by switching to the mid-IR for atmospheric mitigation is the lack of detectors with sufficient speed and sensitivity for long distance communications. Current commercial solutions tend to fall into either of two categories. The first is thermal detectors making use of microbolometers, which can be made relatively cheap. However, these detectors must often trade sensitivity for response time, while high speed optical communication often

#533926 https://doi.org/10.1364/OPTCON.533926
Journal © 2024 Received 25 Jun 2024; revised 25 Aug 2024; accepted 2 Sep 2024; published 11 Sep 2024

OPTICS CONTINUUM

requires both to be maximized. The other category is small bandgap semiconductor materials, such as HgCdTe or InSb. These are commercially available and tend to have much higher bandwidths than thermal detectors. However, the small bandgap leads to high dark currents due to thermal noise that typically require cooling to mitigate. While in some instances Peltier coolers are sufficient for the application, peak performance often requires cryogenic cooling, while SWIR detectors operate well at room temperature by default [4]. Even with this cooling, direct mid-infrared detection is several orders of magnitude below comparable SWIR detectors in terms of detectivity. Detectivity is an important figure of merit classifying the overall performance of a detector and is defined as the inverse of the noise-equivalent power normalized per square root of the sensor's area and frequency bandwidth, with units of Jones ($\text{cm} \cdot \sqrt{\text{Hz}}/\text{W}$). It is a method of directly comparing detectors while controlling for variables that affect detector performance such as active area and the signal frequency. Typical values for state-of-the-art direct SWIR detectors are $10^{13} - 10^{14}$ Jones, while direct mid-infrared detectors have detectivities of $10^{10} - 10^{11}$ Jones [3,5,6].

Mid-infrared upconversion using nonlinear optics stands as an established method of overcoming these limitations. By mixing an intense pump beam with a mid-infrared idler beam inside a nonlinear crystal, the mid-infrared idler can be upconverted to wavelengths in the 700-900 nm range while maintaining the spatial and spectral content of the signal [7]. This coincides with high responsivity silicon detectors which offer lower noise, higher speed, and the potential for room temperature operation over both short bandgap semiconductors as well as InGaAs detectors used in the C-band [5,8]. Before discussing the state-of-the-art for mid-IR upconversion, it is necessary to clarify some important terminology. Throughout this work, there are many references to power conversion efficiency and quantum efficiency (QE). Power conversion efficiency is derived from taking the output upconverted signal power just after the output crystal facet and dividing it by input mid-infrared idler power just before the nonlinear crystal facet:

$$PE = \frac{P_s}{P_i} \tag{1}$$

This is a useful metric for how efficient the overall nonlinear process is. Another important metric for certain applications like imaging and quantum communications is the quantum efficiency. When referring to quantum efficiency, the experimental efficiency can be retrieved from the power efficiency by multiplying by the ratio between the signal and idler wavelengths, converting it to a photon ratio, which is the definition of quantum efficiency:

$$QE = \frac{P_s}{P_i}\frac{\lambda_s}{\lambda_i} \tag{2}$$

Therefore, by Eqs. (1) and (2), we end up with our device's power efficiency of 36% and a quantum efficiency of ~8.5%. There is also a useful formula for the theoretical maximum quantum efficiency derived by Dam et al, who currently hold the intracavity QE record of 20% [9,10]:

$$QE_{max} = \frac{16\pi d_{eff}^2 l^2 P_{Gauss}}{n_1 n_2 n_3 \epsilon_0 c \lambda_1 \lambda_3 w_0^2} \tag{3}$$

where l is the length of the nonlinear crystal, P_{Gauss} is the circulating pump power of Gaussian beam in the cavity, d_{eff} is the effective nonlinear coefficient of the nonlinear medium, n_i is the refractive index of the PPLN for the indicated beam, λ_n is the wavelength for the indicated beam, and w_0 is the beam radius of the pump beam in the center of the PPLN. The main limitation of this formula is that it was derived assuming the pump and idler beams are defocused inside of the nonlinear medium to the point that they can be approximated as plane waves. For devices making use of tightly focused gaussian beams, such as ours, this formula is not applicable. It will

OPTICS CONTINUUM

still serve as a useful formula for suitable devices in the literature, since it estimates the upper limit of quantum efficiency achievable for a certain pump power and upconversion wavelength.

Now that we have clarified the efficiency terms, we can discuss the state of the art for upconversion detectors. This technology is already well established in the SWIR, with upconversion quantum efficiencies >90% used in imaging and single photon counting applications [8,11–14]. Experimentally demonstrated quantum efficiencies for mid-infrared upconversion tend to be lower than the SWIR. This is due to the inherent efficiency loss from converting longer wavelengths and therefore lower energy photons into higher energy ones, as can be seen by the inverse wavelength dependence in Eqs. (2) and (3). This is also due to the difficulty of sourcing high quality mid-IR optics and coatings relative to the SWIR. Another consideration is that for wavelengths longer than 3.6 microns, higher absorption in the mid-infrared in PPLN is to blame. PPLN is often used due to its broad transmission spectrum, but it exhibits increasing absorption past 3.6 microns that limits conversion efficiencies significantly [7,15,16].

There have been a number of interesting developments in the state of the art for mid-infrared upconversion over the last two decades. Starting with bulk crystal intracavity continuous wave devices, much work has been performed by Ajanta Barh, Rasmus Pedersen, Peter Tidemand-Lichtenberg, and Jeppe Dam. As mentioned previously, Dam et al. holds the record for a CW intracavity bulk crystal upconversion detector with a quantum efficiency of 20% [10,17]. Pedersen et al. and Barh. et al. have iterated on this work, deriving thermal noise equivalent power for mid-IR upconversion and demonstrating ultra-broadband mid-IR upconversion using fanned grating PPLN crystals and non-collinear phase matching [7,9,16,18–20]. While this is the experimental record for intracavity bulk crystal devices, higher quantum efficiencies have been demonstrated in the mid-IR using pulsed sources, PPLN waveguides, and high pump power single-pass schemes.

Hogstedt et al. demonstrated a pulsed mid-IR upconversion detector with a signal-to-noise ratio 500 times higher than that of a cryogenically cooled InSb detector, due to the large reduction in dark current from using a Si-based detector [21]. In 2007, Imaki and Kobayashi demonstrated a pulsed upconversion setup with 40% QE, in 2013 Gu et al. achieved 64% QE efficiency using a pulsed setup, and in 2017 Wolf et al. demonstrated up to 82% QE efficiency using very high energy pulses [22–24]. A recent development in April 2024 was quantum entanglement and interference demonstrated at 3 microns by Ge et al [25]. Using a single-pass upconversion scheme in PPLN with 45 W pumping power, they demonstrated 37.9% QE, which is the current record for bulk continuous wave PPLN to the best of our knowledge.

Literature on mid-IR waveguide upconverters is harder to find. This is due to the fact that, until recently, it was difficult to manufacture lithium niobate waveguides with low losses at wavelengths <2.0 μm, preventing efficient upconversion [26–29]. To the best of our knowledge the current state of the art is 85%/W internal SFG efficiency with a pump power of 0.192 W using a PPLN ridge waveguide by Lehmann et al [30]. This corresponds to a QE of 16% derived from values in the paper. This demonstrates that the QE of waveguides can be higher than bulk for much lower pump powers, given the pump powers in the bulk demonstrations are typically tens of watts. All of these structures have applications in mid-infrared imaging, military countermeasures, spectroscopy, remote sensing, gas detection, and free space optical communication, making upconversion a versatile option with a demonstrated record of performance in the literature [3,20,31–34].

In this paper, we aim to fill a gap in the literature identified above. While the general operating principles of upconversion detection are understood, a systematic study utilizing focused gaussian beams has not been presented recently. We present a systematic study on mid-infrared upconversion based on quasi phase matched PPLN in a compact intracavity structure both experimentally and theoretically using tightly focused gaussian beams. We utilize the thermal lens generated by high power pumping of a Nd:YVO_4 gain medium to achieve a smaller

OPTICS CONTINUUM

beam radius in the nonlinear crystal, while making use of a longer nonlinear crystal to maximize conversion efficiency. The 1064 nm light emitted by the Nd:YVO_4 is confined in a cavity and mixed with 3469 nm mid-IR light generated via difference frequency generation using a previously reported laser from our research group [35]. This generates upconverted light at 814.2 nm, and we achieved 9.5 mW of 814.2 nm light for 26.3 mW of 3469 nm mid-IR light. As such, we report a measured upconversion efficiency of 36% and a calculated quantum efficiency of 8.5%. The lowest optical power measured was 150 nW of DFG which corresponded to 53 nW of SFG power, limited by the detection circuit. A theoretical calculation of the noise-equivalent power limit shows a possible floor of $\sim 1.7 \cdot f\mathrm{W}/\sqrt{\mathrm{Hz}}$, enabling single photon counting applications.

While our device does not currently surpass the previous state of the art currently in terms of efficiency, it is quite compact at $3.75 \times 3 \times 8$ cm which is important for free space communication, remote sensing, and other relevant applications. Additionally, we show through detailed theoretical analysis that if certain optimizations are made, it is possible for the device to meet and even exceed the performance bar set by Dam et al. for significantly lower circulating powers inside of the cavity thanks to the focusing of the beams in the PPLN coupled with higher pump powers. We hope that this study will serve as a useful reference point for those looking to create high efficiency mid-infrared upconversion detectors in the future through a solid fundamental understanding of the operating principles.

Following this Introduction, we present in the Methods section the experimental set-up, the cavity design and optimization, the cavity and upconversion simulation work, and the theory for beam overlap. In the Results section, we present the leaking 1064 nm and SFG output power dependence on pump power, show the potential optimization work to be done with the beam overlap, characterize the linearity of the SFG response, measure the stability of the output SFG light, measure the conversion efficiency for various lengths of nonlinear crystal, and determine the temperature response of the upconversion process. In the Discussion section, we calculate the theoretical noise equivalent power for a state-of-the-art silicon detector and discuss the potential optimizations and future work identified in the results section from the experimental and theoretical results.

2. Methods

A schematic diagram of the SFG intracavity setup is shown in Fig. 1.

The setup consists of an 808 nm F-mount diode that is linearly polarized, has an integrated fast-axis collimator, and is capable of up to 10W output power (Focuslight FL0FM01-10-808-Y). This was followed by an Nd:YVO_4 gain medium where the facet facing the 808 LD was coated for high reflection at 1064 nm ($R > 99.9\%$) and high transmission at 808 nm ($T > 95\%$), while the output facet had an anti-reflection coating for 1064 nm ($T > 99.8\%$). A dichroic mirror was used to couple mid-infrared light into the cavity. This mirror was a custom unit fabricated at the National Research Council: it was a 1.8-mm thick N-BK7 substrate coated on both surfaces with high transmission at 1064 nm ($R \sim 99.4\%$), high reflectivity in the mid-infrared ($R > 82.4\%$), and high reflectivity at 808 nm ($R > 99.9\%$) to help reduce leaking 808 nm light. These values were valid only for an angle of incidence of 45° and for s-polarized light. To confirm the filters removed leaking 808 nm light, the output was measured via optical spectrum analyzer down to the nanowatt level. There was no signal at or around 808 nm, and the only signal present was the 814.2 nm light from the upconversion process. The mid-infrared light was generated by a DFG module previously described by our research group [35]. It was coupled into the cavity via two gold-coated mirrors (Thorlabs PF05-03-M01) in a Z-fold configuration, then passed through a 2X beam expander (Thorlabs LA5763-E, LA5817-E) and focusing lens (Thorlabs LA5042-E) in order to achieve the desired focus in the center of the nonlinear crystal. In the future, this setup will be replaced by an appropriate fiber collimator and focusing lens to make the signal arm of the setup more compact.

OPTICS CONTINUUM

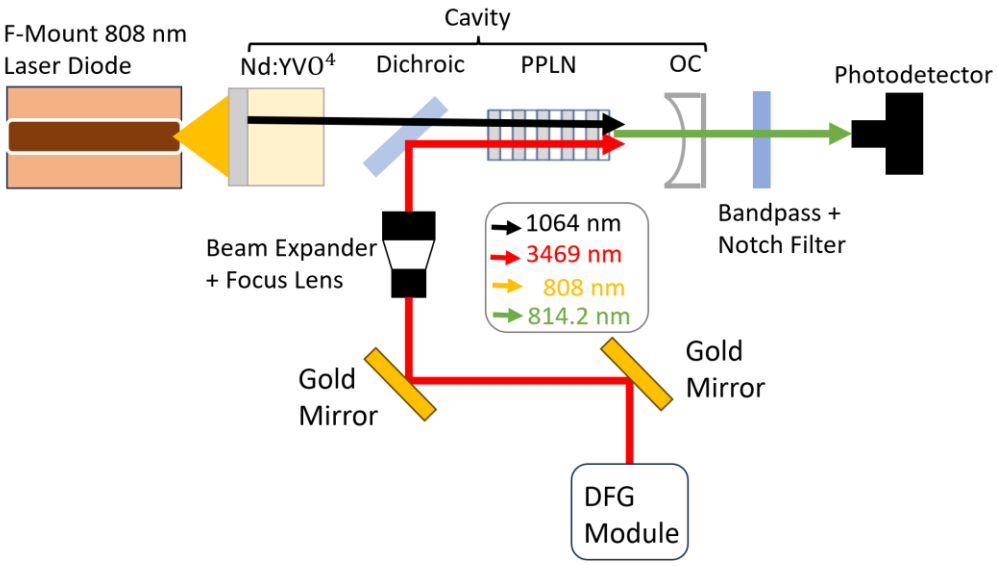

Fig. 1. Experimental schematic diagram of the intracavity SFG laser. The DFG module is described in a previous manuscript from our research group [35].

The nonlinear crystal was a 47.5 mm long periodically-poled 5% MgO-doped lithium niobate crystal (MgO:PPLN) with a period of 22.75 μm that was fabricated in-house by our group. The MgO:PPLN was coated on both facets with an AR coating at 1064 nm (T > 99.8%) and at 3369 nm (T > 95%), while the output facet was also coated for high transmission at the SFG wavelength of 814.2 nm (T > 99%). The MgO:PPLN was mounted to a copper heatsink via thermal compound and temperature controlled via a thermoelectric cooler (TEC) to an accuracy of 0.05 °C. The output coupling mirror (OC) was a custom unit on a Calcium Fluoride substrate that was 6 mm in diameter and had a high reflectivity coating at 1064 nm (R > 99.85%) and high transmission at the SFG wavelength (T > 99.9%). Residual 1064 nm and 3469 nm light was filtered after the OC using a bandpass filter centered at 820 nm with 10 nm FWHM (Thorlabs FBH820-10) and a 1064 nm notch filter (Thorlabs NF1064-44). Measurements above 0.01 mW were captured using a Thorlabs S401C thermal power meter, while measurements below this value were captured using a Thorlabs PDA36A2 variable gain Si detector. The cavity was <8 cm in length measured from the Nd:YVO_4 HR coating to the OC.

A hemispherical cavity was selected due to its relative simplicity and ease of alignment. In order to optimize the pump beam distribution inside of the PPLN, a cavity model was set up using the open-source ReZonator software [36]. This software implements ABCD matrix methods for cavity mode simulations in standing wave and ring resonators. A block diagram of the cavity and a plot of the pump beam evolution inside of the cavity can be seen in Fig. 2. The cavity consists of a plane mirror representing the HR coating of the Nd:YVO_4 (M1) immediately followed by the 5 mm long Nd:YVO_4. To model the effect of thermal lensing, a thin lens F1 is inserted in the middle of the Nd:YVO_4 sample and a thermal lens of 75 mm was found to match the experimental results well, and is in line with prior characterizations of thermal lensing effects in Nd:YVO_4 [37]. The thermal lens is important as it allows us to attain a smaller beam radius in the PPLN for the pump, which increases the efficiency due to the higher intensity. Following the Nd:YVO_4 is a 5 mm gap (d1) and then a 1.8 mm thick plate of N-BK7 representing the dichroic mirror. This is followed by a 10 mm gap (d2) and a 47.5 mm slab of material representing the PPLN. The final gap of 5 mm (d3) leads into the output coupler for the cavity with a radius

OPTICS CONTINUUM

of curvature of 100 mm (OC). In the beam radius plot, the vertical dashed lines represent the location of the thermal lens (blue), the dichroic facets (green), and the PPLN facets (red). A beam radius of ~110 μm is obtained in the center of the PPLN with a symmetric Gaussian profile. The focus for the mid-IR beam in the center of the PPLN was found to be 55 μm.

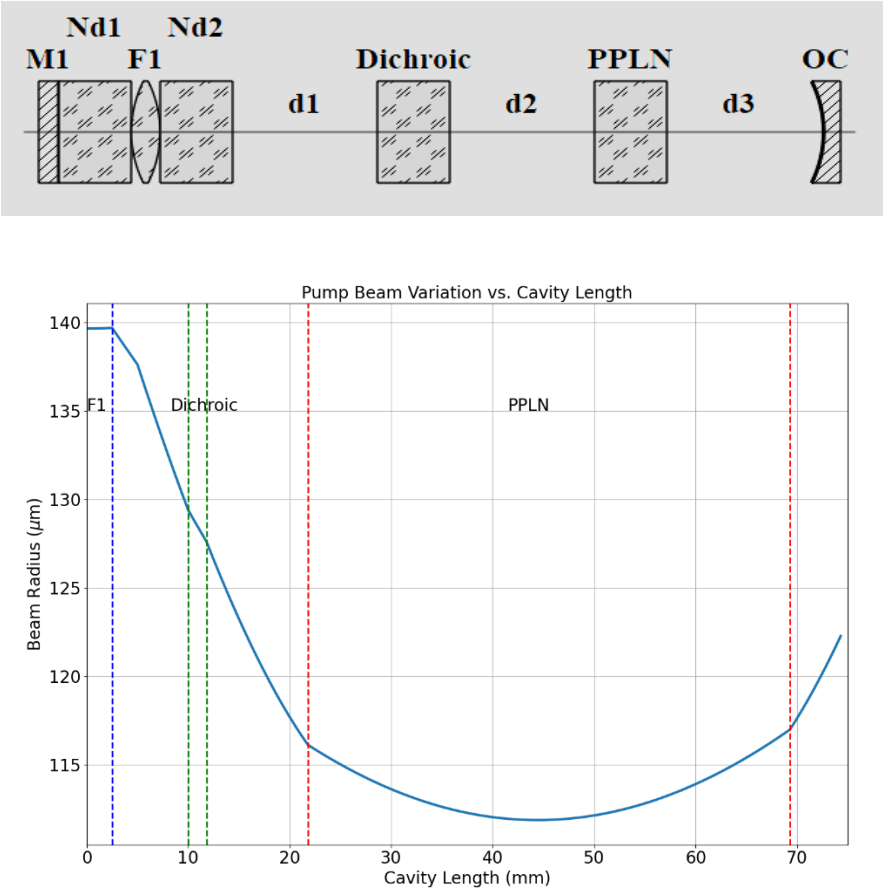

Fig. 2. A block diagram of the cavity model (upper) and a plot of the 1064 nm pump beam radius as it evolves through the cavity left to right (lower). The distance is measured relative to the plane cavity mirror M1.

In order to simulate the expected SFG output power, we first simulated the cavity to estimate the circulating intracavity power, and then used the nonlinear wave equations for SFG to estimate the output power without accounting for beam overlap. This allows us to account for the nonlinear conversion process, which is an additional source of loss within the cavity. Once the SFG power was estimated, a nonlinear loss was calculated and the intracavity simulation was run again. This updates the circulating intracavity power which was then used to generate a new SFG power estimate. This process repeated until the SFG power and intracavity power converged, i.e. the change between iterations was negligible. In this case, the nonlinear loss ends up being negligible as the depletion was negligible, due to the pump intensity being many orders of magnitude higher than both the signal and SFG intensities. Should the signal and SFG intensity approach that of the pump, depletion and thus the nonlinear loss would become noticeable. The cavity simulation is the same as the one presented in our previous work for a DFG intracavity source using a spatially dependent rate equation from Risk, omitted here for brevity [35,38]. The nonlinear

OPTICS CONTINUUM

wave equations are the same as those presented by Boyd [39]:

$$\frac{dA_1}{dz} = \frac{2i\omega_1 d_{\text{eff}}}{k_1 c^2} A_2^* A_3 e^{-i\Delta kz} \tag{4}$$

$$\frac{dA_3}{dz} = \frac{2i\omega_3 d_{\text{eff}}}{k_3 c^2} A_2 A_1 e^{+i\Delta kz} \tag{5}$$

where A_1, A_2, A_3 represent the electric field amplitude of the mid-IR signal, the 1064 nm pump, and the upconverted 814 nm SFG, respectively. d_{eff} is the nonlinear coefficient (14 pm/V typ. for PPLN). Δk is the phase mismatch for SFG where k_i is the wave vector for the indicated wave ($\Delta k = k_1 + k_2 - k_3$), c is the speed of light, ω_i is the optical frequency for the indicated wave, and z is the propagation direction along the optical axis in the nonlinear crystal. In this case, there is no rate equation for the pump A_2, as it is assumed to be high enough in intensity that depletion is negligible and thus A_2 is constant.

Another important consideration for optimizing the output power of the SFG device is the beam overlap inside of the crystal. The most straightforward way to treat this problem for tightly focused gaussian beams is using overlap integrals as covered by Guha and Falk [40,41]. While the treatments are derived for single pass, we have found that using the above cavity simulation to estimate the circulating power coupled with Guha and Falk's approach gives results that agree well with the experimental data. The derivation for the formula itself is several pages and so is omitted here, although it can be found in its entirety in the cited works by Guha and Falk. The general idea is to integrate over the entire plane of the output crystal facet to obtain the output signal power for a given pump and idler power. The result of the derivation is the complex double integral h with many variable terms, found below:

$$\begin{aligned} h &= \left(\frac{1}{4\xi_4}\right) I, \\ I &= \int_0^1 \int_0^1 dz_1 dz_2 \times \frac{\exp[i\Delta kl(z_1 - z_2)] \exp\left[-\left(\frac{4B^2}{\alpha}\right)(z_1 - z_2)^2 f\right]}{(z_1 - A)(z_2 - A_1^*) + C_1} \end{aligned} \tag{6}$$

where

$$\begin{aligned} k &= \frac{k_1}{k_2} \\ B &= \frac{\rho}{2}\left(\frac{l(k_1 + k_2)}{2}\right)^{\frac{1}{2}} \\ \xi_1 &= l/(2z_{R1}) \\ \xi_2 &= l/(2z_{R2}) \\ \xi_3 &= \frac{\xi_1 \xi_2 (1 + k)}{\xi_2 + k\xi_1} \\ \xi_4 &= \frac{\xi_1 + k\xi_2}{1 + k} \\ \alpha &= \frac{\xi_1 + k\xi_2}{(1 + k)\xi_1 \xi_2} \\ A_1 &= \frac{1}{2} + \frac{i}{4}\left(\frac{1}{\xi_3} + \frac{1}{\xi_4}\right) \\ C_1 &= -\frac{1}{16}\left(\frac{1}{\xi_3} - \frac{1}{\xi_4}\right)^2 \\ z_3' &= \frac{1}{2} + \frac{i}{2\xi_3} \end{aligned} \tag{7}$$

OPTICS CONTINUUM

and

$$f = \frac{(z_1 - z_3')(z_2 - z_3'^{*})}{(z_1 - A_1)(z_2 - A_1^{*}) + C_1} \tag{8}$$

where * denotes complex conjugates where appropriate. The resulting integral is $h((\Delta kl),\ \xi_1,\ \xi_2, k, B)$ where (Δkl) represents the phase mismatch for a crystal of length l, with phase mismatch for quasi-phasematching determined by $\Delta k = k_1 + k_2 - k_3 - \frac{2\pi}{\Lambda}$, where $k_i = \frac{2\pi n_i}{\lambda_i}$ and Λ is the period of the periodically poled crystal. ξ_i is the focus factor, found by dividing the length of the crystal by twice the Rayleigh length of the given beam inside of the crystal (also known as the confocal parameter). $k = k_1/k_2$ is the ratio of the wavenumbers of the pump and idler, and B is a term representing the phase walk-off. Since we are using PPLN, $B = 0$ for all cases. By varying the phase mismatch through adjusting the temperature of the PPLN, the value of the integral h can be maximized for a given crystal. By doing this, h is then only a function of the focus factors, allowing us to see how adjusting the size of the beams in the crystal may affect the output power. The goal is to maximize h for a given crystal. This treatment can be found in the results section, as it is relevant to future improvements for the device. The simulation work above is compared to the experimental results in the following section.

3. Results

3.1. Output power characterization

The leaking 1064 nm power was experimentally measured with the dichroic mirror and PPLN crystal in the cavity. This allows accurate characterization of the total cavity loss for the simulation, while also enabling estimation of the circulating intracavity power for PE estimation. Figure 3 shows the experimental results compared with our simulation results. The 1064 nm power is measured after the output coupler and is used to determine the circulating power in the cavity for both the QE calculation and the SFG calculation. To simulate this, the cavity simulation from earlier is used with all known loss values from coatings and other intracavity components accounted for. The agreement between simulation and experiment is good, with the simulation overestimating slightly with respect to the best fit line. This agreement means that we can be confident that the input circulating power estimates for the SFG simulation are accurate with respect to the real cavity setup. For all plots, a 3% error bar is applied, as this was the dominant error from the uncertainty of the Thorlabs S401C photodetector used. However, given the size of the red square markers used to designate the experimental data, these bars are not always visible. In this case, the marker itself is an accurate representation of the experimental error.

After characterization of the circulating 1064 nm power, the next step is to measure and estimate the produced SFG power. The results are shown in Fig. 4, where again we see good agreement between the simulated predictions and the experimental line of best fit. For the simulation work, the cavity power from the simulation is used as input to the nonlinear wave equations and the beam overlap simulation as described in the Methods section. The simulated SFG power is estimated just after the output facet, and so need to be adjusted for the transmission of the OC and filters before the detector. A maximum SFG power of 8.5 mW is measured at the detector and needs to be adjusted for optical filter transmission. The output coupler (T = 99.9%), 1064 nm notch filter (Thorlabs NF1064-44, T = 99.57%), and bandpass filter (FBH820-10, T = 90%) are considered to estimate the SFG power just after the PPLN output facet. The adjusted maximum SFG power obtained just after the PPLN output facet was 9.5 mW for 26.3 mW of input mid-IR power measured just before the PPLN input facet, leading to a measured power efficiency of 36.0%.

OPTICS CONTINUUM

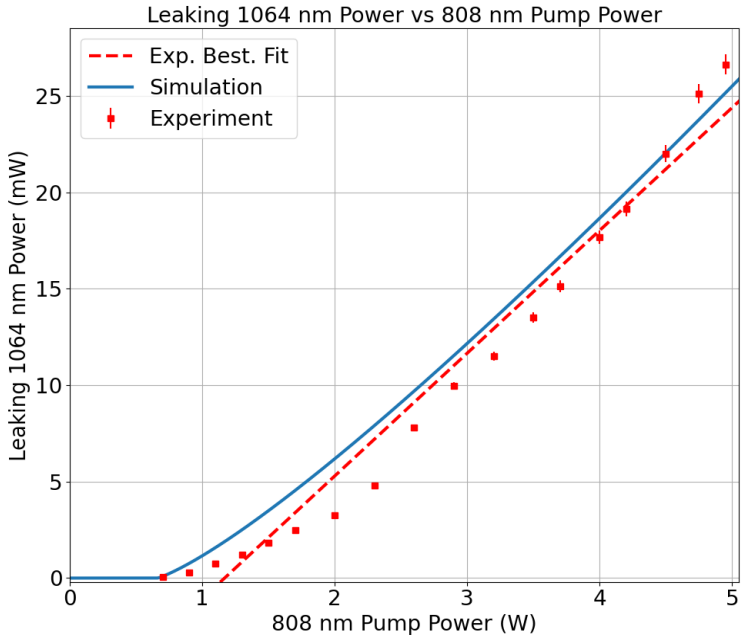

Fig. 3. Measured and simulated leaking 1064 nm power vs 808 nm pump power. Error bars are present on all markers but are smaller than the data markers for most points. The solid blue line is the simulation, while the dashed red line is the line of best fit for the experimental data.

3.2. Beam overlap characterization

Here we evaluate the overlap of the pump and idler beams in the nonlinear crystal, and see if any further improvements could be made. From Eq. (7), the focus factors for the pump and idler for refractive indices of 2.15 and 2.08 and beam radii of 110 μm and 55 μm are $\xi_1 = 0.31$ for the 1064 nm pump and $\xi_2 = 4.2$ for the idler, respectively. This shows that the idler beam is overfocused while the pump beam could be focused further, and so there is room for improvement in terms of device efficiency. In practice, further focusing of the pump beam is difficult to achieve with the hemispherical cavity, as cavity simulation suggests further decreasing the beam size in the PPLN would require a larger thermal lens, which could lead to significant cavity instability. However, since a different cavity design could theoretically be utilized, we will examine two cases. First, we will look at the value of h for the current device and see how changing the idler focus factor could lead to further efficiency gains. We will then calculate a second curve for h assuming an ideal pump beam in the nonlinear crystal as well, with a target focus factor of 2.3. In the following discussion, the pump focus factor is assumed fixed since we cannot significantly change the focus factor for the current cavity design. Both curves have been optimized for ideal phase matching as well. The results can be found below in Fig. 5:

We can see that there are significant efficiency gains that could be made to the current device structure. Starting with the blue curve representing the current device and the fixed pump focus factor of 0.31, the current value of h is 0.385 for $\xi_2 = 4.2$. However, since the idler beam is overfocused, we could relax the beam focusing such that we hit the maximum value of h, which is 0.541 at a idler focus factorof $\xi_2 = 1.39$ (or a radius of 94 microns vs the current 55). This alone would correspond to an increase in efficiency of $\sim\frac{0.541}{0.385} = 40.5\%$, increasing the power efficiency and quantum efficiency to 50.6% and 11.9% respectively. This will require reconfiguring the focus lens and collimator used for the idler arm of the experiment, which can be

OPTICS CONTINUUM

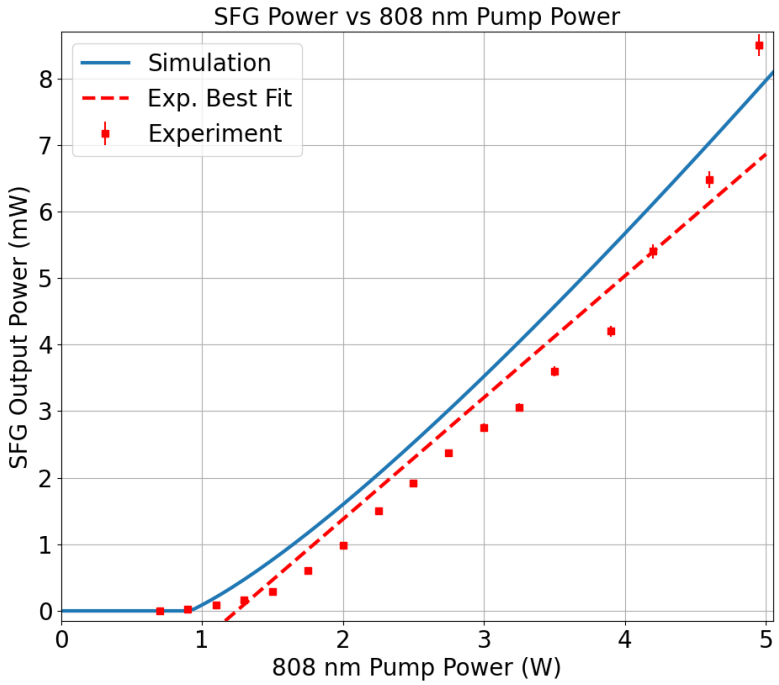

Fig. 4. Measured and simulated output SFG power vs 808 nm pump power. Error bars are present on all markers but are smaller than the data markers for most points. The solid blue line is the simulation, while the dashed red line is the line of best fit for the experimental data.

accomplished by using a lower power focusing lens, which we do not currently have to perform this experiment.,That being said, it is otherwise a straightforward change to make. A harder change is optimizing the pump beam, as achieving the target focus factor of 2.3 requires a pump beam radius of 40 microns. Using ReZonator, there are no configurations that can achieve such a small beam size in the PPLN while retaining the compact hemispherical cavity. However, if we assume an equally compact alternate cavity design is possible, the maximum value of h is 0.735 with an idler focus factor of 1.58 (or an idler radius of 88 microns). In this case, that would represent a total efficiency gain of 91% over the current device, with theoretical power and quantum efficiencies of 68.8% and 16.1% respectively. This is for a circulating power of 17W, which is about 6 times lower than that required for Dam et al's record quantum efficiency of 20%, which required 100W of circulating power in the cavity. On paper, if we were to apply this circulating power to the theoretical optimized device, quantum efficiencies >90% seem possible. Despite this, an important consideration that our treatment lacks are the effects of temperature and intense focusing inside of the nonlinear medium. Tightly focused gaussian beams for cavity powers as high as Dam et al's could potentially lead to significant thermal effects if not outright damage to the crystal, which is a concern that would require more detailed modelling to overcome. One possible work-around is to move to a pulsed regime, where intensities can be maximized for short periods of time, limiting the potential for damage. A recent example of this is from Huang et al. in 2021, where they utilized ultrafast lasers to achieve a quantum efficiency of 80% in the mid-infrared [42]. Additionally, there are trade-offs to using tightly focused gaussian beams depending on the application. Tighter focuses inside of the nonlinear medium coupled with longer crystals significantly limits the field of view (FOV), which can be limiting for imaging and remote sensing applications. As our target domain is optical satellite communication, the

OPTICS CONTINUUM

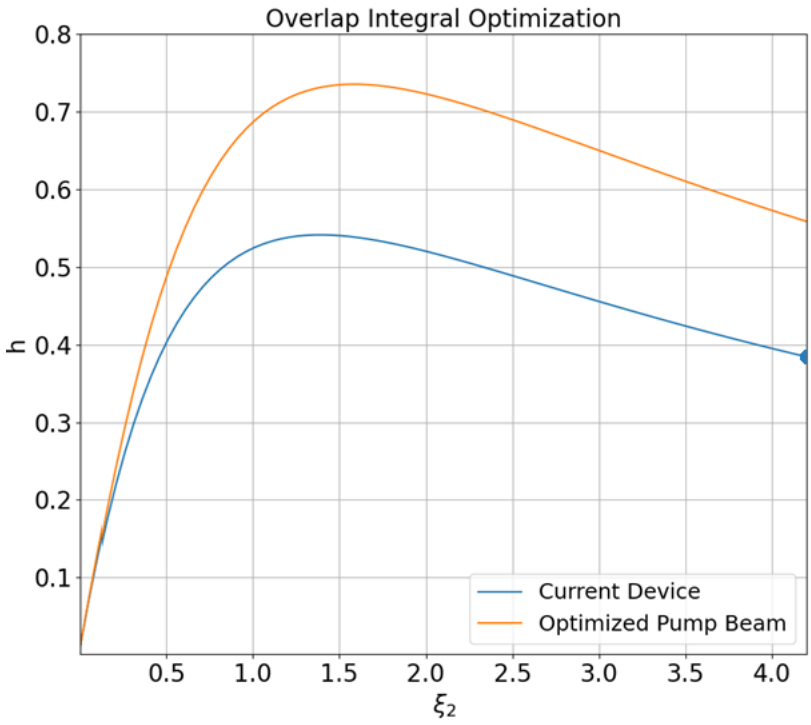

Fig. 5. A plot of the overlap integral for the current device (blue curve) as well as a hypothetical fully optimized device (orange curve). The current device efficiency is marked with the blue circle. We can see that there are significant efficiency gains to made with the current device even if the pump beam is not changed due to cavity design restrictions.

FOV is already quite low compared to other domains, and so this is less of a concern. It still bears repeating however and it shows that tightly focused gaussian beams, while potentially more efficient, are not always a suitable solution.

3.3. Device linearity and limit of detection

An important practical and theoretical consequence of upconversion is that the SFG output power should have a linear dependence with respect to input mid-IR signal power. It is important to validate this, as linear responses are typically desirable for photodetectors, and a nonlinear response would introduce additional difficulties when using the device. To ensure linearity, the SFG power was measured as a function of input mid-IR light power. Then, we produce a log-log plot using base 10 logarithms and fit a linear curve to the data. In theory, the closer the slope of the curve is to 1, the more confident we can be that the y variable depends linearly on the x variable. The results are plotted in Fig. 6, where we can see the equation for the line of best fit is $y = 1.0059x - 0.5864$. As our slope is quite close to 1, we can confidently say that the SFG upconversion demonstrates a linear dependence on the input mid-IR signal power.

We also tested the limit of detection using the equipment on hand. The lowest power we measured was 53 nW (-42.8 dBm) of SFG corresponding to ~150 nW of DFG. The results are plotted in units of dBm in Fig. 7 to demonstrate the continued linearity on the low end of the power scale. The error bars represent a 3% error from the detector and an additional flat error from the limited precision of the oscilloscope used to read the output voltage from the detector (~2 mV). This is why the error bars get more pronounced with decreasing magnitude of the

OPTICS CONTINUUM

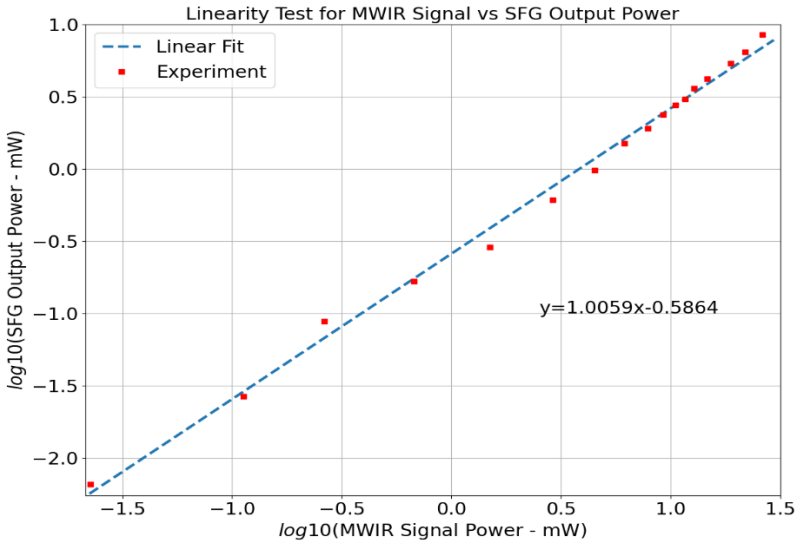

Fig. 6. A base 10 log-log plot of the SFG power dependency on the input signal power. This is done to check linearity, as in theory the closer the slope of the line of best fit to 1, the more confidently we can say the SFG has a linear dependence on input mid-IR power.

measured power. While the selected photodetector could detect lower powers than this, we ran into issues with electronic noise introduced by the old model of oscilloscope being used for the readings. A full re-design of the detector circuit using more modern components would allow us to provide an experimental demonstration of the practical limit of detection. As we currently lack the equipment to measure the limit of detection, a theoretical value for the noise equivalent power for this detector can be found in the Discussion, alongside other important noise considerations.

3.4. *Length dependence*

Since our group has in-house PPLN fabrication capabilities, several lengths of PPLN were produced with the same period of 22.75 μm. Each sample was tested to see if the measured conversion efficiency deviated from the theoretical expectation, and to test the variability in PPLN quality between samples. The results are shown in Table 1 below.

Table 1. Nonlinear Crystal Length Dependence Results

PPLN Length (mm)	Measured Power Efficiency (%)	Length Corrected Power Efficiency (%)	Nonlinear Conversion Efficiency per unit length (%/W-cm)
35	25.34	34.39	1.61
43	31.13	34.38	1.61
47.5	36.0	36.0	1.69

We see that, as expected, the conversion efficiency drops with nonlinear crystal length. For the third column, "length corrected" refers to adjusting each crystal's conversion efficiency by the ratio between the crystal length with respect to the longest crystal. For example, to adjust the second sample, the conversion efficiency is multiplied by $\frac{47.5}{43} = 1.10$ to correct it, since SFG power is linearly proportional to PPLN length for small mid-IR intensities [43]. In theory, if all PPLN are identical, then the corrected conversion efficiencies would be identical. We can see some variance in the corrected conversion efficiencies, though they are all within ~1.6% of the

OPTICS CONTINUUM

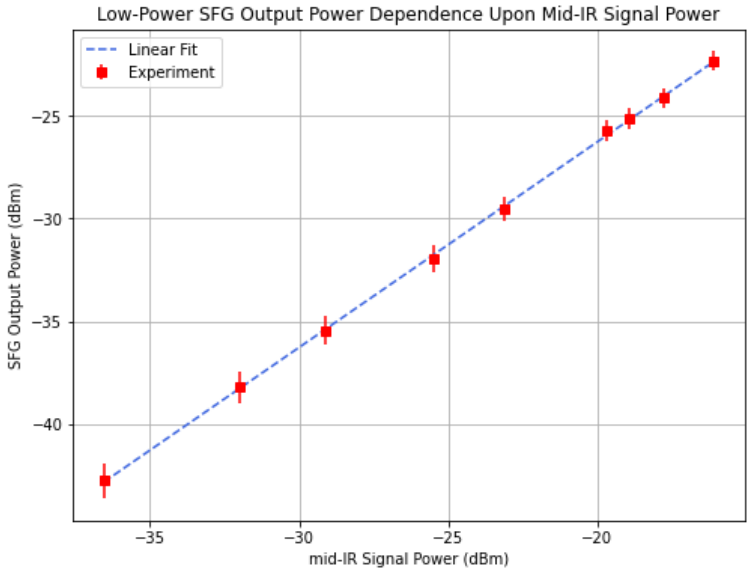

Fig. 7. A plot in dBm showing the lowest powers detected in our experiments. In theory much lower powers can be detected, but the detection electronics proved to be insufficient for this purpose. A theoretical discussion of the limit of detection is included in the discussion as a result.

expected value of 36%. This can be attributed to manufacturing errors in the PPLN coupled with variations in alignment caused by removing and inserting different PPLN samples repeatedly. This is also shown with the conversion efficiency per unit length in the final column, which was found by dividing the SFG power by the product of the input idler power and the 808 nm pump power used. In a well-poled crystal, there is minimal dependence on crystal thickness, so long as the crystal is thick enough to fully contain both the pump and idler beams to avoid beam clipping. However, manufacturing errors during the domain inversion of the crystal could lead to imperfect poling (i.e. not vertical with respect to the input beam), and poling may not be uniform in the direction perpendicular to the input beam, leading to a position dependence as well. On top of this, lithium niobate does not have a high thermal conductivity, meaning the closer the beam is to the surface of the PPLN, the better the thermal dissipation is. All of this can account for potential differences between PPLN samples. The main takeaway is that there is no significant difference between any of the PPLN samples tested, and longer crystals directly lead to higher power efficiencies as expected.

3.5. Stability and beam profile

Stability over time is another important metric for an optical instrument. To test this, the DFG module was held at a constant input power while the SFG measurement was allowed to run freely for two hours with no adjustments. The SFG power was measured over this two-hour period, and then the stability is calculated as the root mean square deviation of the SFG dataset. The experimental measurements are plotted in Fig. 8. To keep the number of data points reasonable, the SFG power was sampled every 30 seconds during the two-hour experiment. Typical stability values for nonlinear DPSS-based lasers are 1-4% [12,44,45]. The stability of the SFG upconversion was found to be 3.75% after 2 hours, which is in line with this range. The dip in power around 140 samples is due to a sudden drop in power from the DFG input module

OPTICS CONTINUUM

because of instability from using an unpolarized 808 nm pump source and is not due to a change in performance from the SFG module.

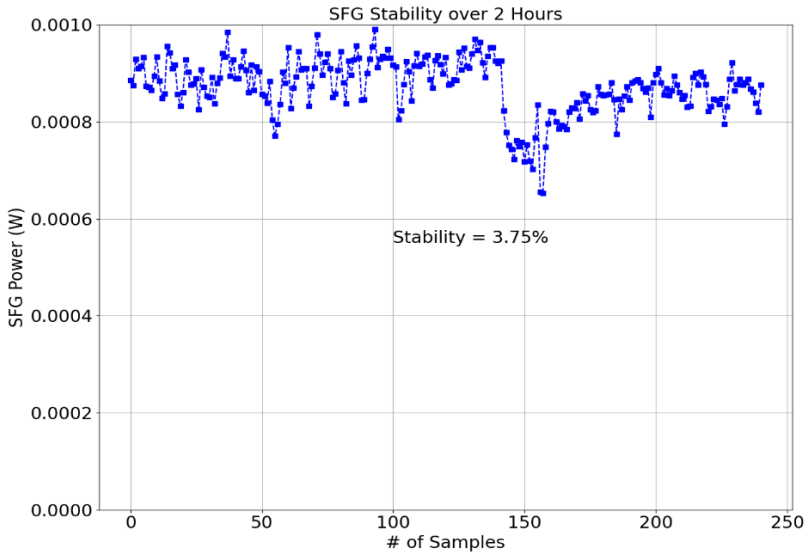

Fig. 8. The measured SFG power fluctuations over a two-hour period to determine stability. Each sample represents a 30 second interval, after which SFG power was measured.

3.6. Temperature dependence

Finally, the temperature dependence of the SFG power was measured to ensure the poling period was accurate and the developed mid-IR detector has sufficient temperature tolerance for practical applications. Experimentally, the temperature of the PPLN was varied by 1 degree increments, tracing out a temperature tuning curve. In the simulation, the temperature dependence of the refractive index of the lithium niobate was modelled using Sellmeier equations [46]. The results can be seen in Fig. 9. The FWHM of the experimental curve is ~8 degrees Celsius, while the theoretical curve fits well. 8 degrees Celsius temperature tolerance should be sufficient for most of the practical applications. In general, there is good agreement, although the peak is slightly off from the experimental value, perhaps due to experimental error and not allowing enough time for the crystal to reach thermal equilibrium. We see that focused gaussian beam theory can also account for the elongated "tail" on the left-hand side of the experimental data. This is a well-known phenomenon that occurs when one or both of the pump and idler beams deviate from plane wave behavior and begin to transition into focused gaussian beams. This can also be due to ellipsoidal beams or tip/tilt misalignment of one or both beams with respect to the optical axis [39–41]. In our case, it is likely due to strong focusing of the idler beam and moderate focusing of the pump, leading to a confocal parameter smaller than the length of the nonlinear crystal. If a broader temperature response is required, the use of chirped nonlinear gratings will help at the cost of conversion efficiency [43]. Alternatively, Barh et al. demonstrated ultra-broadband mid-IR upconversion by physically translating a fanned grating PPLN crystal to achieve upconversion from 3.6–4.85 microns in the mid-IR [16,19].

OPTICS CONTINUUM

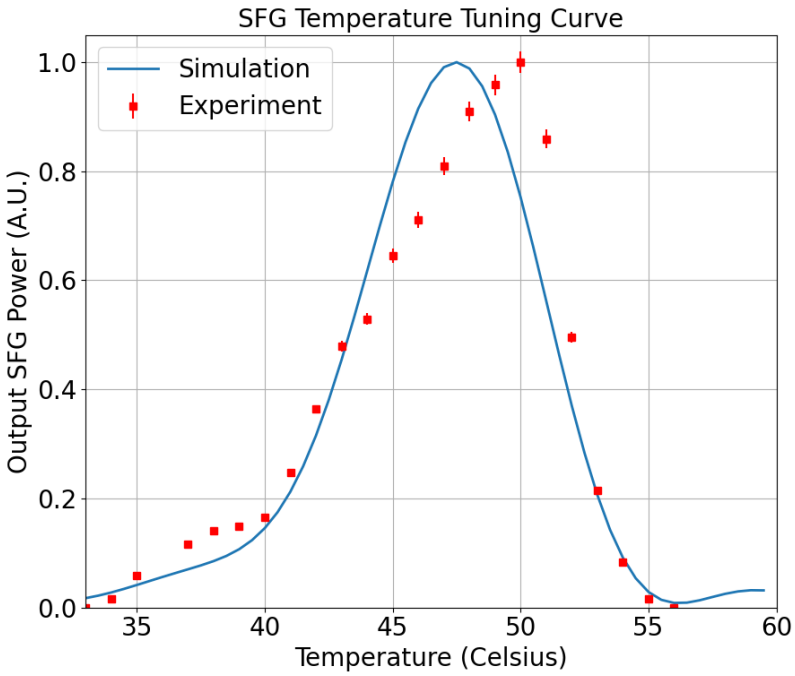

Fig. 9. Theoretical temperature tuning curve calculated via Sellmeier equations compared to experimental data. The solid blue line is simulated while the red dots are experimental data.

4. Discussion

The results show that we have achieved a power conversion efficiency of 36% (QE 8.5%) with good agreement to a theoretical treatment using focused gaussian beams. We also see that the main area for improvement is in the overlap between pump and idler, with a potential 40% gain to be implemented by defocusing of the idler beam. This will be implemented in a future iteration after simulating the appropriate focus lens and fiber collimator to pair with the signal, as in the future we anticipate the idler beam originating from a fiber-coupled source. This alone raises the PE to 50.6% (QE 11.9%), and we've seen a fully optimized pump beam could theoretically push the device to a PE of 68.8% (QE 16.1%). This is for an 808 pump power of 5W and a circulating power of 17W 1064 nm, which means comparable performance to Dam et al's intracavity conversion record of 20% with significantly less circulating power required. One potential way to surpass the intracavity record set by Dam et al. would be to increase the 808 nm pump power, as the Nd:YVO4 easily supports 10W pumping. Assuming a linear relation, this would double the circulating 1064 nm power and thus the efficiency, meaning that our current device with an optimized idler beam could reach a PE of 101.2% (QE 23.8%), and a fully optimized cavity redesign might reach a PE of 137.6% (QE 32.1%) which would represent a new experimental record. Another method of improving the efficiency would be optimization of the cavity itself, mainly by improving the coatings further on any intracavity components. Simulation work suggests this could lead to further improvement of the circulating 1064 nm power for a given 808 nm pump, although the coatings are already performing well so this may not be worth the cost. Regardless of the selected path forward, there is significant work to be done to implement this, and there may be additional problems like the aforementioned thermal effects that limit the total efficiency. However, the theoretical analysis is promising and shows

OPTICS CONTINUUM

that there is a possibility for our device to meet and even exceed the current state of the art for intracavity upconversion detectors, which is an exciting avenue for future work. Of course, for readers interested in developing improved mid-IR upconverters, the FOV required by the intended application must be considered heavily as well, as focused beams do limit FOV heavily.

The noise properties of upconversion detection are important as well. While we currently lack the necessary equipment to present a detailed treatment of upconversion noise considerations, this has been covered thoroughly in the literature. Specifically, Pedersen et al. and Barh et al. have theoretically and experimentally determined the various noise limits due to thermal considerations, SPDC, and other relevant phenomena [7,18,20]. Another consideration is phase noise and intensity noise, which is relevant depending on the modulation format used, given the device is intended for free space communication. This requires characterization of the power spectral density of the phase noise, typically using an RF spectrum analyzer. Unfortunately, we do not currently have access to this equipment, which is why the treatment is missing from this study. We hope to perform this in a future study alongside gigabit modulation detected via upconversion. However, Gray et al. and Tawfieq et al. performed a similar analysis for an upconversion detector in 2020, and so interested readers can refer to their manuscript for a breakdown on the contributions from shot noise, relative intensity noise, and other phenomena [47,48].

Another important metric for upconversion detection is the effective noise-equivalent power (NEP) achievable in the mid-infrared via the use of upconversion detection. As one might expect, higher conversion efficiencies lead to lower effective NEPs, which can broadly be considered an increase in sensitivity for a given measurement bandwidth. First, we must characterize the NEP limit from the upconversion process alone. This has been extensively derived by Pedersen et al. and Barh et al. and can be calculated from the following formula [7,18]:

$$NEP = \frac{\sigma E_p \omega_{IR}}{\omega_{up}\eta_{up}\sqrt{\Delta f}} \tag{9}$$

where E_p is the energy per photon, η_{up} is the upconversion efficiency, σ is the square root of the mean number of events for a Poisson distribution, Δf is the frequency bandwidth, and ω represents the mid-IR and upconverted optical frequencies. Now that the upconversion NEP is known, we must consider two different regimes for potential detector set-ups. The first is represented by the formula above, and is valid when the electronic noise of the detector is negligible relative to the magnitude of the upconversion NEP. In the second, the electronic noise in the detector dominates, and the NEP of the upconversion setup can be estimated as:

$$NEP = \frac{\omega_{IR}}{\omega_{up}\eta_{up}} NEP_{det} \tag{10}$$

We can see both cases have the same dependence on upconversion efficiency. Our quantum efficiency may be 42% that of the record set by Dam et al., but it can still produce a respectable NEP. Using previous estimates by Pedersen et al. as a baseline, our device is theoretically capable of a floor for upconversion noise of $\sim 1.7 \cdot f\mathrm{W}/\sqrt{\mathrm{Hz}}$. This would be for upconversion at 810 nm with an integration time of 1 second [18]. This is still suitable for a number of high sensitivity applications and outcompetes direct mid-infrared detection with low-bandgap semiconductor materials.

Another goal of this work was to make the mid-IR detector more compact to enable portable remote sensing and gas detection applications. The current cavity length is <8 cm and is mainly limited by the length of the PPLN. As we tested multiple lengths of PPLN, we have shown that PE values >25% can be maintained for crystal lengths as low as 35 mm, so there is potential to reduce this further depending on the specific application needs. We are also currently pursuing professional packaging in-house, and we have machined a prototype module with dimensions

OPTICS CONTINUUM

of $3.75 \times 3.0 \times 8.0$ cm. Through redesigning the optical lens train coupling the mid-infrared light into the cavity according to the findings of the simulation work, we hope to reduce this further in the future. This should allow an upconversion module to be used in a wide variety of applications where a portable, high quality room temperature mid-infrared detector is needed. We also hope to demonstrate a mid-infrared free space optical link in atmosphere as part of the High Throughput Secure Networks program in Canada. This is part of a broader goal to demonstrate gigabit speed mid-infrared communication for atmospheric mitigation purposes and will be explored in more detail in future work from our group.

5. Conclusion

In conclusion, we have demonstrated a compact intracavity SFG upconversion with an experimental power efficiency of 36.0% (quantum efficiency 8.5%). This was achieved in a compact packaged form factor of $3.75 \times 3.0 \times 8.0$ cm, making it suitable for remote sensing, free space communication, and other applications where a compact, high speed, high sensitivity mid-infrared detector is required. The experiment generated a maximum upconverted output power of 9.5 mW of 814.2 nm for 26.3 mW of input 3469 nm light using bulk PPLN. The experimental results agree well with theoretical predictions from cavity simulations and focused gaussian beam theory. This has been achieved using a novel linear cavity design to for ease of alignment and to minimize size. Given the short time scale of nonlinear optical phenomena, the input mid-IR signal could be modulated at high speed to enable a new class of detectors for mid-IR optical communication links. In future work, we hope to improve the device efficiency considerably according to the optimizations identified by the simulation work, which could lead to almost double the power and quantum efficiency for the same pump power. We also aim to demonstrate long-distance communication at gigabit signal rates using a high-speed modulated mid-infrared source to further emphasize the usefulness of this module for free space optical communication. The module also has other applications in mid-infrared spectroscopy, gas detection, autonomous vehicle LIDAR, imaging, and more.

Funding. High Throughput and Secure Networks Challenge Program (HTSN-621, HTSN-644); Natural Sciences and Engineering Research Council of Canada (RGPIN-2018-05501).

Acknowledgment. The authors thank the National Research Council of Canada for help identifying collaborators for this work.

Disclosures. The authors declare no conflict of interest.

Data availability. Data underlying the results presented in this paper are available from the authors upon reasonable request.

References

1. A. Trichili, M. A. Cox, B. S. Ooi, *et al.*, "Roadmap to free space optics," J. Opt. Soc. Am. B **37**(11), A184–A201 (2020).
2. E. Leitgeb, T. Plank, M. S. Awan, *et al.*, "Analysis and evaluation of optimum wavelengths for free-space optical transceivers," in *2010 12th International Conference on Transparent Optical Networks* (2010), pp. 1–7.
3. L. Flannigan, L. Yoell, and C. Xu, "Mid-wave and long-wave infrared transmitters and detectors for optical satellite communications—a review," J. Opt. **24**(4), 043002 (2022).
4. A. Rogalski, P. Martyniuk, M. Kopytko, *et al.*, "Trends in Performance Limits of the HOT Infrared Photodetectors," Appl. Sci. **11**(2), 501 (2021).
5. A. Rogalski, "Infrared detectors: an overview," Infrared Phys. Technol. **43**(3-5), 187–210 (2002).
6. P. Martyniuk, J. Antoszewski, M. Martyniuk, *et al.*, "New concepts in infrared photodetector designs," Appl. Phys. Rev. **1**(4), 041102 (2014).
7. A. Barh, P. J. Rodrigo, L. Meng, *et al.*, "Parametric upconversion imaging and its applications," Adv. Opt. Photonics **11**(4), 952–1019 (2019).
8. R. Demur, R. Garioud, A. Grisard, *et al.*, "Near-infrared to visible upconversion imaging using a broadband pump laser," Opt. Express **26**(10), 13252–13263 (2018).
9. J. S. Dam, C. Pedersen, and P. Tidemand-Lichtenberg, "Theory for upconversion of incoherent images," Opt. Express **20**(2), 1475–1482 (2012).

OPTICS CONTINUUM

10. J. S. Dam, P. Tidemand-Lichtenberg, and C. Pedersen, "Room-temperature mid-infrared single-photon spectral imaging," Nat. Photonics **6**(11), 788–793 (2012).
11. H. Pan, H. Dong, H. Zeng, *et al.*, "Efficient single-photon counting at 1.55μm by intracavity frequency upconversion in a unidirectional ring laser," Appl. Phys. Lett. **89**(19), 191108 (2006).
12. H. Pan and H. Zeng, "Efficient and stable single-photon counting at 1.55 μm by intracavity frequency upconversion," Opt. Lett. **31**(6), 793–795 (2006).
13. T.-H. Wong, J. Yu, Y. Bai, *et al.*, "Sensitive infrared signal detection by upconversion technique," Opt. Eng. **53**(10), 107102 (2014).
14. M. Mathez, P. J. Rodrigo, P. Tidemand-Lichtenberg, *et al.*, "Upconversion imaging using short-wave infrared picosecond pulses," Opt. Lett. **42**(3), 579–582 (2017).
15. P. Tidemand-Lichtenberg, M. Aagaard, A. S. Ashik, *et al.*, "Tunable infrared upconversion module for the 1.9 to 5.5 μm range," Opt. Lett. **47**(23), 6189–6192 (2022).
16. A. Barh, C. Pedersen, and P. Tidemand-Lichtenberg, "Ultra-broadband mid-wave-IR upconversion detection," Opt. Lett. **42**(8), 1504–1507 (2017).
17. Y. Li, Y. He, Y. Wang, *et al.*, "Ultra-sensitive mid-wavelength-infrared upconversion detector," Opt. Laser Technol. **168**, 109993 (2024).
18. R. L. Pedersen, L. Høgstedt, A. Barh, *et al.*, "Characterization of the NEP of mid-infrared upconversion detectors," IEEE Photonics Technol. Lett. **31**(9), 681–684 (2019).
19. A. Barh, M. Tawfieq, B. Sumpf, *et al.*, "Upconversion spectral response tailoring using fanout QPM structures," Opt. Lett. **44**(11), 2847–2850 (2019).
20. A. Barh, P. Tidemand-Lichtenberg, and C. Pedersen, "Thermal noise in mid-infrared broadband upconversion detectors," Opt. Express **26**(3), 3249–3259 (2018).
21. L. Høgstedt, J. S. Dam, A.-L. Sahlberg, *et al.*, "Low-noise mid-IR upconversion detector for improved IR-degenerate four-wave mixing gas sensing," Opt. Lett. **39**(18), 5321–5324 (2014).
22. M. Imaki and T. Kobayashi, "Infrared frequency upconverter for high-sensitivity imaging of gas plumes," Opt. Lett. **32**(13), 1923–1925 (2007).
23. X. Gu, K. Huang, H. Pan, *et al.*, "Efficient mid-infrared single-photon frequency upconversion detection with ultra-low background counts," Laser Phys. Lett. **10**, 055401 (2013).
24. S. Wolf, T. Trendle, J. Kiessling, *et al.*, "Self-gated mid-infrared short pulse upconversion detection for gas sensing," Opt. Express **25**(20), 24459–24468 (2017).
25. Z. Ge, Z.-Q.-Z. Han, F. Yang, *et al.*, "Quantum entanglement and interference at 3 μm," Sci. Adv. **10**(10), eadm7565 (2024).
26. A. Shams-Ansari, G. Huang, L. He, *et al.*, "Reduced material loss in thin-film lithium niobate waveguides," APL Photonics **7**(8), 081301 (2022).
27. L. Cai, Y. Wang, and H. Hu, "Low-loss waveguides in a single-crystal lithium niobate thin film," Opt. Lett. **40**(13), 3013–3016 (2015).
28. Y. Zhang, Q. Luo, S. Wang, *et al.*, "On-chip ytterbium-doped lithium niobate waveguide amplifiers with high net internal gain," Opt. Lett. **48**(7), 1810–1813 (2023).
29. M. Bazzan and C. Sada, "Optical waveguides in lithium niobate: Recent developments and applications," Appl. Phys. Rev. **2**(4), 040603 (2015).
30. L. Lehmann, L. Grossard, L. Delage, *et al.*, "Single photon MIR upconversion detector at room temperature with a PPLN ridge waveguide," Opt. Express **27**(14), 19233–19241 (2019).
31. P. Colarusso, L. H. Kidder, I. W. Levin, *et al.*, "Infrared Spectroscopic Imaging: From Planetary to Cellular Systems," Appl. Spectrosc. **52**(3), 106A–120A (1998).
32. A. Sijan, "Development of military lasers for optical countermeasures in the mid-IR," in *Technologies for Optical Countermeasures VI* (SPIE, 2009), Vol. 7483, pp. 32–45.
33. Y. J. Kaufman and L. A. Remer, "Detection of forests using mid-IR reflectance: an application for aerosol studies," IEEE Trans. Geosci. Remote Sensing **32**(3), 672–683 (1994).
34. D. Richter, A. Fried, and P. Weibring, "Difference frequency generation laser based spectrometers," Laser Photonics Rev. **3**(4), 343–354 (2009).
35. L. Flannigan, A. Atwi, T. Kashak, *et al.*, "Compact diode-pumped solid-state laser with intracavity pump-enhanced DFG emitting at ~3.5 microns," Photonics **10**(10), 1164 (2023).
36. N. I. Chunosov, "reZonator," http://rezonator.orion-project.org/.
37. I. O. Musgrave, W. A. Clarkson, and D. C. Hanna, "Detailed study of thermal lensing in Nd:YVO/sub 4/ under intense diode end-pumping," in Technical Digest. Summaries of Papers Presented at the *Conference on Lasers and Electro-Optics. Postconference Technical Digest* (IEEE Cat. No.01CH37170) (2001), pp. 171–172.
38. W. P. Risk, "Modeling of longitudinally pumped solid-state lasers exhibiting reabsorption losses," J. Opt. Soc. Am. B **5**(7), 1412–1423 (1988).
39. R. Boyd, *Nonlinear Optics*, 4th ed. (Academic Press, n.d.).
40. S. Guha and J. Falk, "The effects of focusing in the three-frequency parametric upconverter," J. Appl. Phys. **51**(1), 50–60 (1980).
41. S. Guha, J. O. Barnes, and L. P. Gonzalez, "Multiwatt-level continuous-wave midwave infrared generation using difference frequency mixing in periodically poled MgO-doped lithium niobate," Opt. Lett. **39**(17), 5018–5021 (2014).

OPTICS CONTINUUM

42. K. Huang, Y. Wang, J. Fang, *et al.*, "Mid-infrared photon counting and resolving via efficient frequency upconversion," Photonics Res. **9**(2), 259–265 (2021).
43. S. M. M. Friis and L. Høgstedt, "Upconversion-based mid-infrared spectrometer using intra-cavity $LiNbO_3$ crystals with chirped poling structure," Opt. Lett. **44**(17), 4231–4234 (2019).
44. N. Savage, "Ultraviolet lasers," Nat. Photonics **1**(2), 83–85 (2007).
45. G. Dudzik, J. Sotor, K. Krzempek, *et al.*, "Single-frequency, fully integrated, miniature DPSS laser based on monolithic resonator," Proc. SPIE **8959**, 89591F (2014).
46. O. Gayer, Z. Sacks, E. Galun, *et al.*, "Temperature and wavelength dependent refractive index equations for MgO-doped congruent and stoichiometric LiNbO3," Appl. Phys. B **91**(2), 343–348 (2008).
47. A. C. Gray, S. A. Berry, L. G. Carpenter, *et al.*, "Upconversion detection of 1.25 Gb/s mid-infrared telecommunications using a silicon avalanche photodiode," Opt. Express **28**(23), 34279–34289 (2020).
48. M. Tawfieq, A. K. Hansen, O. B. Jensen, *et al.*, "Intensity noise transfer through a diode-pumped titanium sapphire laser system," IEEE J. Quantum Electron. **54**(1), 1–9 (2018).